



HAL
open science

Three-Dimensional Modeling of Anion Exchange Membrane Electrolysis: A Two-Phase Flow Approach

Erwan Tardy, Yann Bultel, Florence Druart, Antoine Bonnefont, Melaine Guillou, Benoit Latour

► **To cite this version:**

Erwan Tardy, Yann Bultel, Florence Druart, Antoine Bonnefont, Melaine Guillou, et al.. Three-Dimensional Modeling of Anion Exchange Membrane Electrolysis: A Two-Phase Flow Approach. *Energies*, 2024, 17 (13), pp.3238. 10.3390/en17133238 . hal-04674996

HAL Id: hal-04674996

<https://hal.science/hal-04674996v1>

Submitted on 22 Aug 2024

HAL is a multi-disciplinary open access archive for the deposit and dissemination of scientific research documents, whether they are published or not. The documents may come from teaching and research institutions in France or abroad, or from public or private research centers.

L'archive ouverte pluridisciplinaire **HAL**, est destinée au dépôt et à la diffusion de documents scientifiques de niveau recherche, publiés ou non, émanant des établissements d'enseignement et de recherche français ou étrangers, des laboratoires publics ou privés.

Article

Three-Dimensional Modeling of Anion Exchange Membrane Electrolysis: A Two-Phase Flow Approach

Erwan Tardy ^{1,2}, Yann Bultel ^{1,*}, Florence Druart ¹, Antoine Bonnefont ¹, Melaine Guillou ² and Benoit Latour ²

¹ Univ. Grenoble Alpes, Univ. Savoie Mont Blanc, CNRS, Grenoble INP, LEPMI, F-38000 Grenoble, France; erwan.tardy@grenoble-inp.fr (E.T.); florence.druart@grenoble-inp.fr (F.D.); pierre-antoine.bonnefont@grenoble-inp.fr (A.B.)

² Manufacture Française des Pneumatiques Michelin, 23, Place des Carmes, F-63040 Clermont-Ferrand, France; melaine.guillou@michelin.com (M.G.); benoit.latour@michelin.com (B.L.)

* Correspondence: yann.bultel@grenoble-inp.fr

Abstract: Anion exchange membrane water electrolyzers (AEMWEs) are attracting growing interest as a green hydrogen production technology. Unlike proton exchange membrane (PEM) systems, AEMWEs operate in an alkaline environment, allowing one to use less expensive, non-noble materials as catalysts for the reactions and non-fluorinated anion exchange polymer membranes. However, the performance and stability of AEMWEs strongly depend on the alkaline electrolyte concentration. In this work, a three-dimensional multi-physics model considering two-phase flow effects is applied to understand the impact of KOH electrolyte concentration and its flow rate on AEMWE performance, as well as on the current and gas volume fraction distributions. The numerical results were compared to experimental data published in the literature. For current densities above 1 A/cm², a strongly non-uniform H₂ and O₂ gas volume distribution could be evidenced by the 3D simulations. Increasing the KOH electrolyte flow rate from 10 to 100 mL/min noticeably improves cell performance for current densities above 1 A/cm². These results show the importance of accounting for the three-dimensional geometry of an AEMWE and two-phase flow effects to accurately describe its operation and performance.

Keywords: anion exchange membrane water electrolysis; three-dimensional model; two-phase flow; KOH concentration



Citation: Tardy, E.; Bultel, Y.; Druart, F.; Bonnefont, A.; Guillou, M.; Latour, B. Three-Dimensional Modeling of Anion Exchange Membrane Electrolysis: A Two-Phase Flow Approach. *Energies* **2024**, *17*, 3238. <https://doi.org/10.3390/en17133238>

Academic Editor: Giovanni Esposito

Received: 30 May 2024

Revised: 21 June 2024

Accepted: 26 June 2024

Published: 1 July 2024



Copyright: © 2024 by the authors. Licensee MDPI, Basel, Switzerland. This article is an open access article distributed under the terms and conditions of the Creative Commons Attribution (CC BY) license (<https://creativecommons.org/licenses/by/4.0/>).

1. Introduction

As a high-potential energy carrier, hydrogen can be used for both storing and regulating electricity generated from renewable sources. Hydrogen has also attracted attention since it can replace fossil energies for various industrial applications that significantly contribute to greenhouse gas (GHG) emissions, such as the steel industry and fertilizer production. Green hydrogen produced through water electrolysis from renewable electricity is a promising solution to decarbonizing these sectors. Among the low-temperature water electrolysis technologies, membrane electrolyzers have received substantial attention, allowing for high purity hydrogen production at high current densities, compact cell design, and dynamic operation at high differential pressure [1,2].

There are two types of membrane electrolyzers: proton exchange membrane water electrolyzers (PEMWEs) and anion exchange membrane water electrolyzers (AEMWEs). PEM technology has benefited from intensive research for several years. Its operation in an acidic environment allows high current densities to be reached (>2 A/cm² for applied voltages below 2 V) [3]. In addition, PEM technology is well adapted to load variations, which is particularly suitable for renewable energy storage. PEMs are predominantly made from a polyfluoroalkyl polymer (PFAS), which exhibits good mechanical and thermal stability due to its very stable carbon-fluorine bonds. However, PFAS is problematic as it is highly toxic and polluting with low degradation and high soil/water contamination [4].

Thus, growing interest has been focused on AEMWE technology operating in an alkaline environment, which allows for the use of non-precious and/or less expensive metals as catalysts, diffusion layers, and bipolar plates. Among these, nickel (Ni) and its iron (Fe)-, cobalt (Co)-, or aluminum (Al)-based alloys are predominantly used. However, these catalysts do not achieve the desired performance [5,6]. Therefore, it is necessary to use thicker catalytic layers and a supply with an alkaline electrolyte, usually KOH or NaOH, to achieve similar current densities [7]. Furthermore, unlike PEM systems, there is a wide variety of non-fluorinated anion exchange polymer membranes (AEMs) with lower environmental impact than the ones used in acidic technologies [8]. Despite recent progress, there is a development lag of AEMWE systems compared to others [1]. It is necessary to notably increase their lifespan and improve their ability to operate at high currents. A significant increase in electrode overpotentials is observed in high-current domains, lowering energy efficiency and potentially compromising the durability of electrolyzers. It is indeed under these high-current conditions that we observe significant gas evolution of dihydrogen and dioxygen, which can lead to a limitation of electrochemical reactions by mass transport [2]. It is therefore essential to study two-phase flows in order to better understand the bubble formation process and the transport of H₂ and O₂ bubbles and their impact on reaction mechanisms. For example, it has been shown that bubbles dispersed in the electrolyte of AEMWEs hinder the proper migration of hydroxide ions (OH⁻), thereby reducing the effective conductivity of the electrolyte [9]. In addition to preventing ions from reaching the reaction surface, bubbles attached to it lead to a non-uniform distribution of current density, affecting the charge transfer process in these regions [10,11]. Effective bubble removal is thus linked to the wettability and hydrophilicity properties of the materials used. Electrochemical kinetics at interfaces are thus directly influenced by flows in the layer, which can cause heterogeneities and strong local gradients if mismanagement of these flows is observed. The formation, release, and transport of bubbles are complex phenomena. They depend not only on gas interactions with the liquid phase but also with the solid matrix (support/catalyst/ionomer), which can locally modify the microstructure and porosity of the layer, highlighting the importance of the nature of the materials used and their properties. To date, there is a lack of understanding of these phenomena [12], especially in AEM electrolyzers [13]. The strong attractiveness of this technology (which has been growing rapidly in recent years) necessitates improving our understanding of its operation. Moreover, it remains challenging to experimentally observe these phenomena [14–16]. Characterizing two-phase flows is therefore fundamental for studying reaction processes; the strong couplings between charge transfer kinetics at interfaces and mass transport make the study complex [17].

To date, a lot of physics-based models have been developed for alkaline water electrolyzers [18] to analyze their performance, but only a few are dedicated to AEMWEs. An et al. [19] and Lui et al. [20] developed a through-plane 1D model that couples mass transport, charge transport, and electrochemical reactions in an AEMWE. Very recently, Lawand et al. [21] developed a 3D model of a membrane electrode assembly (MEA) composed of Ni Raney at the cathode and NiFe₂O₄ at the anode. The influence of several parameters, such as the electrolyte pH, the membrane, and electrode thicknesses, was investigated.

In this work, a modeling approach of a full AEMWE cell is proposed to evaluate the impact of gas production at both electrodes. Our 3D model is based on the previous 1D model from Liu's work [20] and coupled multiphysics transports with electrochemical reactions. It provides a more accurate description of the actual geometry of the electrolyzer, the electrodes, flow channels, and membrane, and an improved description of the mass transport processes (flow pattern and concentration gradient). Nonuniformities in the current density, O₂ and H₂ production, and concentration can also be considered in 3D simulations. A two-phase flow approach allows one to investigate the impact of the transport of gas in the channel and the porous media, namely, the catalyst layer where hydrogen and oxygen gas evolution take place. Finally, the influence of KOH concentration and the electrolyte flow rate is investigated.

2. Model Description

2.1. Mathematical Modeling

A 3D, continuum, two-phase, isothermal model was developed to study the impact of KOH concentration and flow rate on AEM electrolysis performance. In the following sections, we introduce all of the physics implemented in the model. The AEM electrolyzer model is developed by considering the following assumptions:

1. The fluid mixture is assumed to have Newtonian properties;
2. A homogeneous flow is considered in the channels, which means that the gas and liquid velocities are equal;
3. No-slip condition is assumed at the free-porous interface on the free-flow side, which means that the tangential component of the mixture velocity is set to zero;
4. The oxygen (O₂) and hydrogen (H₂) produced are considered to be present as pure gas bubbles dispersed within the continuous liquid electrolyte;
5. The gas and KOH aqueous electrolyte flows are assumed to be laminar due to the low flow velocity and small pressure gradient;
6. Hydrogen and oxygen crossover through the membrane are neglected;
7. The porous media are isotropic, and the transport phenomena occurring within them are characterized using effective properties;
8. The electrochemically active surface area is assumed to be in contact with the ionomer phase and therefore to be constant whatever the KOH concentration.
9. The ionic conductivity of the ionomer is assumed to depend on the KOH concentration.
10. An isothermal model is assumed.

2.2. Multiphase Flow

The multiphase flow is studied for both liquid and gas in the channels and porous media. The mass transport of the phase k is described for each phase $k \in l, g$.

$$\nabla \cdot (\rho_k \mathbf{u}_k) = R_k \quad (1)$$

where ρ_k and \mathbf{u}_k are the density and velocity of phase k , respectively. Here, R_k represents the mass source term of phase k , which is zero in all of the layers except in the catalyst layers (Table 1).

Table 1. Source terms for mass conservation (Equation (1)).

Component	Gas	Liquid
ACL ¹ (positive electrode)	$+\frac{i_v}{4F}M_{O_2}$	$+R_{ml} M_{H_2O}$
CCL ² (negative electrode)	$-\frac{i_v}{2F}M_{H_2}$	$+R_{ml} M_{H_2O}$

¹ ACL: anode catalyst layer, ² CCL: cathode catalyst layer.

The liquid electrolyte is assumed to drive the gas in the channels. Consequently, the gas and liquid velocities are considered to be equal by neglecting any drift velocity and considering that both phases share the same pressure. A mixture model is then implemented for coupling the mass phase transport (Equation (1)) and the total mass (Equation (2)) and momentum (Equation (3)) transport of the mixture as a single-phase continuum flow with macroscopic properties.

$$\nabla \cdot (\rho_m \mathbf{u}_m) = 0 \quad (2)$$

$$\rho_m (\mathbf{u}_m \cdot \nabla) \mathbf{u}_m = \nabla \cdot \left[-p\mathbf{I} + \mu_m \left(\nabla \mathbf{u}_m + (\nabla \mathbf{u}_m)^T \right) - \frac{2}{3} \mu_m (\nabla \cdot \mathbf{u}_m) \mathbf{I} \right] \quad (3)$$

where p and I are the total pressure and identity matrix, respectively. Here, ρ_m and μ_m represent the mixture density and dynamic viscosity determined by volume-averaging (Equations (4) and (5)).

$$\rho_m = \sum_k s_k \rho_k \quad (4)$$

$$\mu_m = \sum_k s_k \mu_k \quad (5)$$

where s_k is the volume fraction of phase k .

The flow velocity u_k of each phase k is performed by the extended Darcy's law in the porous media.

$$u_k = -\frac{k_{r,k}}{\mu_k} k_{sat} \nabla p_k \quad (6)$$

where $k_{r,k}$ and k_{sat} are the relative and absolute (or saturated) permeabilities. The relative permeability is given by the third power of the volume fraction of each phase.

$$k_{r,k} = s_k^3 \quad (7)$$

The absolute permeability is based on the Kozeny–Carman equation for porous media.

$$k_{sat} = \frac{1}{16} d_{CK}^2 \frac{\varepsilon^3}{k_{CK}(1-\varepsilon)^2} \quad (8)$$

where d_{CK} , k_{CK} , and ε represent the characteristic diameter, an empirical geometric constant, and the porosity, respectively (Table 2).

Table 2. Components, phases present, and material properties taken from [20].

			AEM	ACL	CCL	APTL ²	CPTL ³	CHANNEL
Phases present ¹	-	-	I	i, g, l, e	i, g, l, e	g, l, e	g, l, e	g, l
Porosity	ε	-	0	0.4	0.4	0.4	0.8	1
Ionomer volume fraction	ε_i	-	1	0.15	0.15	0	0	0
Electronically conductive volume fraction	ε_e	-	0	0.45	0.45	0.6	0.2	0
Characteristic diameter	d_{CK}	μm	0	0.25	0.25	7.6	7.6	0
Empirical constant	k_{CK}	-	0	9.375	9.375	4.06	4.06	0

¹ i: ionic, e: electronic, g: gas, l: liquid. ² APTL: anode porous transport layer, ³ CPTL: cathode porous transport layer.

The pressure difference between liquid and gas in the porous media was determined by computing the capillary pressure, p_c , according to the Leverett J-function, $J(s_l)$.

$$p_c = \sigma \cos(\theta) \left(\frac{\varepsilon}{k_{sat}} \right) J(s_l) \quad (9)$$

$$J(s_l) = \begin{cases} 1.417 (1 - s_l) - 2.120 (1 - s_l)^2 + 1.263 (1 - s_l)^3 & \text{for } \theta < 90^\circ \\ 1.417 s_l - 2.120 s_l^2 + 1.263 s_l^3 & \text{for } \theta > 90^\circ \end{cases} \quad (10)$$

where σ and θ are the surface tension and contact angle, respectively (Table 3).

Table 3. Material and electrochemical properties used in the model taken from [20,22].

Symbol	Parameter	Values	Unit
σ	surface tension	66.24	mN/m
θ	contact angle	50	°
σ_e^{bulk}	bulk electronic conductivity [20]	120	S/cm
ξ	electroosmotic coefficient [20]	1	-
α	charge transfer coefficient for reduction	OER: 0.5 HER: 0.5	-

Table 3. Cont.

Symbol	Parameter	Values	Unit
β	charge transfer coefficient for oxidation	OER: 0.5 HER: 0.5	-
IEC	ion exchange capacity	2.353	mmol/g
\bar{V}_l	molar volume of liquid water	18.307	mL/mol
μ_l	viscosity of liquid water [20]	$0.00175 \exp\left(-\frac{16,000}{R} \frac{1}{\text{mol}} \left(\frac{1}{T_t} - \frac{1}{T}\right)\right)$	Pa·s
μ_g	viscosity of gas	$O_2 : 2.026 \times 10^{-5}$ $H_2 : 8.789 \times 10^{-6}$	Pa·s
ρ_l	density of liquid water	983.2	kg/m ³
ρ_g	density of gas	$\frac{P_g}{RT} M_i$ i: O ₂ (anode), H ₂ (cathode)	kg/m ³
$c_{OH^-,ref}$	reference hydroxide concentration	0.1	M
z^-	charge of hydroxide ions	-1	-
P_{ref}	reference pressure	1	atm
P_t	triple point pressure [22]	611.2	Pa
T	operating temperature	60	°C
T_t	triple point temperature [22]	273.16	K
H_l	enthalpy of liquid water [22]	0	J/g
$C_{p,l}$	heat capacity of liquid water [22]	4.217	J/(g·K)
M_{H_2O}	molar mass of water	18	g/mol
M_{O_2}	molar mass of dioxygen	32	g/mol
M_{H_2}	molar mass of dihydrogen	2	g/mol
k_{ml}	constant for absorption and desorption of liquid water [22]	1	g·mol/(cm ³ ·s·J)

2.3. Charge Transport

Electron transport in the electronically conducting phase as the ion transport in the ionomer phase (membrane and catalyst layer) was studied using Ohm's law. The resulting conservation equations for the charge transport are presented in Equations (11)–(13).

$$\begin{aligned} \nabla \cdot i_i &= \nabla \cdot \left(-\sigma_i^{\text{eff}} \nabla \Phi_i - \frac{\sigma_i^{\text{eff}} \xi}{z^- F} \nabla \mu_{H_2O,i} \right) = i_v \quad \text{CLs} \\ \nabla \cdot i_e &= \nabla \cdot (-\sigma_e^{\text{eff}} \nabla \Phi_e) = -i_v \quad \text{CLs} \end{aligned} \quad (11)$$

$$\nabla \cdot i_i = \nabla \cdot \left(-\sigma_i \nabla \Phi_i - \frac{\sigma_i \xi}{z^- F} \nabla \mu_{H_2O,i} \right) = 0 \quad \text{membrane} \quad (12)$$

$$\nabla \cdot i_e = \nabla \cdot (-\sigma_e^{\text{eff}} \nabla \Phi_e) = 0 \quad \text{PTLs} \quad (13)$$

where i is the current density. The subscripts i and e denote ionic and electronic, respectively. Φ and σ represent the potential and conductivity, respectively. Here, ξ and z^- are the electroosmotic coefficient and charge of hydroxide ions (Table 3) and i_v is the volumetric reaction current. The kinetics will be discussed in more detail in the following section. The second term of the conservation equation of the ion transport corresponds to the contribution of the chemical potential of water absorbed in the ionomer phase, $\mu_{H_2O,i}$ [20]. Finally, the conductivities in the porous layers were corrected using the Bruggeman correlation to consider the tortuosity.

$$\sigma_i^{\text{eff}} = \sigma_i^{\text{bulk}} \varepsilon_i^{1.5} \quad (14)$$

$$\sigma_e^{\text{eff}} = \sigma_e^{\text{bulk}} \varepsilon_e^{1.5} \quad (15)$$

Here, the superscripts *eff* and *bulk* denote the effective and bulk conductivity, respectively. ε_i and ε_e are the volume fraction of the ionomer phase and electronically conductive phase (Table 2).

2.4. Electrochemical Reactions

Water is reduced during the hydrogen evolution reaction (HER) at the cathode while the oxygen evolution reaction (OER) occurs at the anode. The OER and HER kinetics were implemented into the model according to the Butler–Volmer equation.

$$i_{v,a} = s_l a_v i_0^{\text{OER}} \left[\left(\frac{c_t}{c_{\text{OH}^-,\text{ref}}} \right)^1 \exp\left(\frac{\beta F}{RT} \eta\right) - \left(\frac{p_{\text{O}_2}}{p_{\text{ref}}} \right)^1 \exp\left(-\frac{\alpha F}{RT} \eta\right) \right] \quad \text{at the anode} \quad (16)$$

$$i_{v,c} = s_l a_v i_0^{\text{HER}} \left[\left(\frac{c_t}{c_{\text{OH}^-,\text{ref}}} \right)^1 \left(\frac{p_{\text{H}_2}}{p_{\text{ref}}} \right)^{0.5} \exp\left(\frac{\beta F}{RT} \eta\right) - \exp\left(-\frac{\alpha F}{RT} \eta\right) \right] \quad \text{at the cathode} \quad (17)$$

where the subscripts a and c denote anodic and cathodic, respectively. α and β represent the charge transfer coefficient for oxidation and reduction, both assumed to be equal to 0.5. F is Faraday's constant, R —universal gas constant, and T —temperature. Note that the volumetric current is positive at the anode and negative at the cathode. a_v refers to the active catalyst surface area per unit volume of the catalyst layer and i_0 , the exchange current densities. Both the anodic and cathodic exchange current densities are the ones measured for commercial IrO_2 (Premion[®]) and PtRu/C (HiSPEC[®] 12100) catalysts [20] and depend on the hydroxide concentration, c_{OH^-} (Table 4). c_t is the concentration of the fixed positive charge in the ionomer, which determines the hydroxide concentration to maintain charge electroneutrality.

$$c_t = \frac{\rho_i}{EW} \varepsilon_i \quad \text{with } EW = 1/IEC \quad (18)$$

$$z^- c_{\text{OH}^-} + z^+ c_t = 0 \quad (19)$$

in which ρ_i , EW and IEC represent the density of the ionomer, the equivalent weight of the polymer electrolyte, and the ion exchange capacity, respectively (Table 3). z^+ is the positive charge. η is the overpotential in the Butler–Volmer equation, which is evaluated from the electronic and ionic potentials.

$$\eta = \Phi_e - \Phi_i - E_{\text{eq}} \quad \text{with } E_{\text{eq}} = \begin{cases} 1.23 - 0.9 \times 10^{-3}(T - 298) & \text{at the anode} \\ 0 & \text{at the cathode} \end{cases} \quad (20)$$

where E_{eq} and T are the equilibrium potential and temperature. The volume fraction of the liquid phase is considered in the Butler–Volmer equation to consider the reduction in active surface area caused by gas production [22].

Table 4. Parameter values as a function of the hydroxide concentrations taken from [20].

Symbol	Parameter	Values					Unit
c_{OH^-}	Hydroxide concentration	0.01	0.02	0.1	0.5	1	mol/L
σ_i	Ionic ionomer conductivity	23.8	32.2	40.8	51.1	57.4	mS/cm
i_0^{OER}	Exchange current density for OER	0.00242	0.00354	0.0129	0.0172	0.0256	mA/cm ²
i_0^{HER}	Exchange current density for HER	0.3439	0.4523	0.6067	0.7894	0.8885	mA/cm ²
a_v	Electrocatalyst specific surface area ¹	1.3×10^7	1.3×10^7	1.3×10^7	1.3×10^7	1.3×10^7	m ² /m ³

¹ Fitted for $c_{\text{OH}^-} = 1$ mol/L for validation by comparing the numerical polarization curves with experimental data obtained in ref. [20] at high current.

2.5. Water Transport through the Ionomer

Water transport in the ionomer is governed by electroosmosis, ion migration, and diffusion [20,23].

$$N_{\text{H}_2\text{O},i} = -\frac{\sigma_i \xi}{z^- F} \nabla \Phi_i - \left(\alpha_1 + \frac{\sigma_i \xi^2}{z^- 2F^2} \right) \nabla \mu_{\text{H}_2\text{O},i} \quad (21)$$

where $N_{\text{H}_2\text{O},i}$ represents the water flux through the ionomer and $\mu_{\text{H}_2\text{O},i}$ represents the chemical potential of water absorbed in the ion-conducting phase. Here, α_1 corresponds to the liquid-equilibrated water transport coefficient [22].

$$\alpha_1 = \frac{k_{\text{sat}}}{\mu_1 \bar{V}_1^2} \varepsilon_i^{1.5} \quad (22)$$

in which \bar{V}_1 is the molar volume of liquid water. A full liquid equilibration is considered, which means that the volume fraction of absorbed water in the ionomer is equal to its maximum value, i.e., for water activity equal to unity. The resulting conservation equation for water transport through the ionomer is presented in Equation (23).

$$\nabla \cdot N_{\text{H}_2\text{O},i} = R_{\text{H}_2\text{O}} - R_{\text{ml}} \quad (23)$$

where $R_{\text{H}_2\text{O}}$ represents the rate of water production at the anode and water consumption at the cathode.

$$R_{\text{H}_2\text{O}} = + \frac{i_{v,a}}{2F} \text{ at the anode } R_{\text{H}_2\text{O}} = + \frac{i_{v,c}}{F} \text{ at the cathode} \quad (24)$$

The rate of water absorption or desorption from the ionomer to the liquid phase, R_{ml} , is assumed to be proportional to the chemical potential difference:

$$R_{\text{ml}} = \frac{k_{\text{ml}}}{M_{\text{H}_2\text{O}}} (\mu_{\text{H}_2\text{O},i} - \mu_{\text{liq}}) \quad (25)$$

in which $M_{\text{H}_2\text{O}}$ and k_{ml} are the molar mass of water and the rate constant for water transfer from the ionomer to the liquid phase. μ_{liq} corresponds to the chemical potential of liquid water [22]:

$$\mu_{\text{liq}} = H_l M_{\text{H}_2\text{O}} \left(1 - \frac{T}{T_t} \right) + C_{p1} M_{\text{H}_2\text{O}} \left(T - T_t - T \ln \left(\frac{T}{T_t} \right) \right) + \bar{V}_1 (p_l - p_t) \quad (26)$$

where H_l , C_{p1} , T_t , and p_t represent the enthalpy and heat capacity of liquid water and the temperature and pressure at the triple point, respectively (Table 3). Note that water vapor is not considered in the model, which means that the gases produced are pure and perfectly dry and that adsorption and desorption only occur between the liquid phase and the ionomer phase.

2.6. Boundary Conditions

Regarding laminar flows through the channels, a total KOH solution flow rate of 100 mL/min for the base case was applied to the inlet of the 24 channels at both the cathode and anode while a relative pressure equal to zero was set at the outlet of each channel (Figure 1). In addition, a free-porous interface boundary condition was used to couple the free and porous media flow between the channels/GDL interface at both sides with a ratio of free flow volume fraction equal to the unity between the phase saturation on the porous side and the phase volume fraction on the free-flow side. As mentioned in hypothesis 3, the no-slip condition is assumed at the free-porous interface on the free-flow side, which means that the tangential component of the mixture velocity is set to zero. No flux is considered on exterior boundaries where no mass flows in or out of the boundaries, which means that the total flux is zero. Finally, the electronic potential Φ_e was set to 0 V at the cathode land/GDL boundary, i.e., between the channels at the interface of the cathode GDL and bipolar plate (not represented in the model) and to the applied cell potential (from 1.4 to 2 V) at the anode land/GDL boundary, i.e., between the channels at the interface of the anode GDL and bipolar plate (not represented in the model).

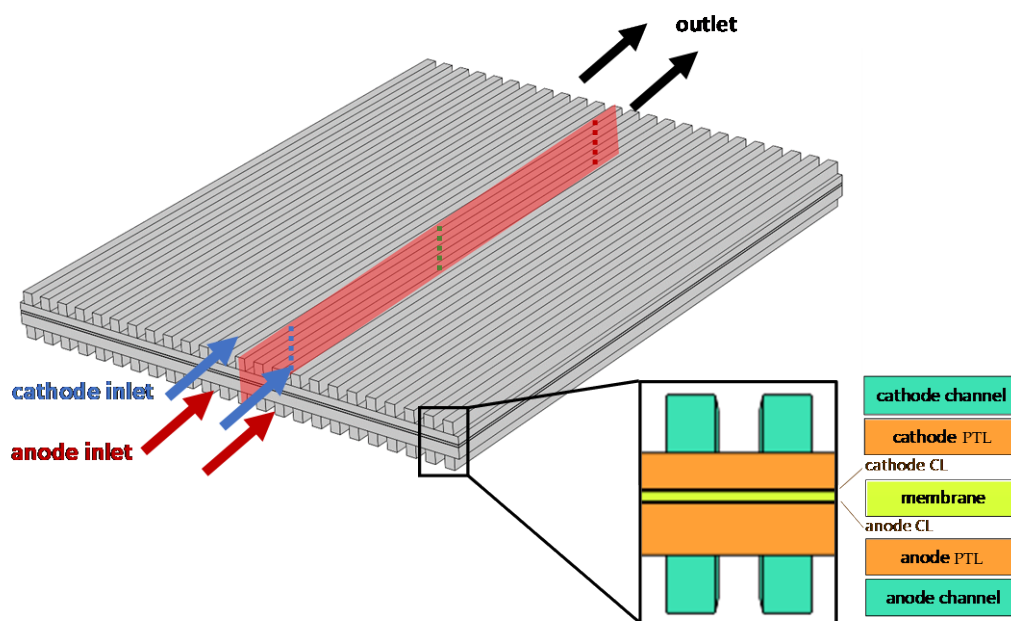


Figure 1. Computational domain of the AEMWE model and its components. The red zone represents a through-plane cut at the middle of the cell. The blue, green, and red dashed lines represent cut lines to obtain numerical distributions from the catalyst layer/membrane interface through the anode and cathode CL thickness for the inlet, middle, and outlet of the cell, respectively. Inlet, middle, and outlet correspond to 10%, 50%, and 90% of the cell length according to the flow direction of the KOH solution, respectively.

2.7. Numerical Procedure

Figure 1 shows the computational domain of the AEMWE model, its components and the mesh configuration. The AEM cell of $1.2 \times 1.5 \text{ cm}^2$ is composed of 24 straight channels on both sides for supplying KOH solution, two porous transport layers (PTLs) and catalyst layers (CLs), and one anion exchange membrane. This cell geometry is the one we are developing for our future experiments. The model dimensions are presented in Table 5. All of the simulations were conducted at $60 \text{ }^\circ\text{C}$ and ambient pressure for different KOH concentrations from 0.01 to 1 M with a flow rate of 100 or 10 mL/min to both sides. All of the governing equations were solved by using version 6.2 of COMSOL Multiphysics[®] software. A residual gas saturation of 1% was assumed in all layers for modeling convenience. The mesh is composed of 46,880 hexahedral elements. The calculation time is about 2 h 30 on Intel[®] Core[™] i5-10505 CPU @ 3.20 GHz to obtain one polarization curve. A grid-independent validation was performed by using different level of finite element mesh refinement and similar results were obtained. The grid-independent validation can be found in Supplementary Material.

Table 5. Dimensions of the modeling domains.

Parameter	Values	Unit
Cell width	12	μm
Channel length	15	μm
Channel height	300	μm
Channel width	250	μm
Rib width	250	μm
CPTL thickness	190	μm
APTL thickness	270	μm
CL thickness	10	μm
Membrane thickness	50	μm

3. Results and Discussion

3.1. Model Calibration and Validation

The ability of the 3D AEMWE cell model to simulate the impact of KOH on cell performance is first validated through comparison of the simulation results with the experimental data published by Liu et al. [20]. The polarization curves computed with the 3D model (solid lines) and experimental data (symbols) obtained for various KOH concentrations ranging from 0.01 to 1 M at 60 °C and 1 atm are presented in Figure 2. The specific surface area was numerically calibrated to fit the experimental results obtained by Liu et al. [20] for a KOH concentration of 1 M (purple symbols in Figure 2) at high current (Table 3). The same specific surface area is considered for the other KOH concentrations as this parameter does not change with the KOH concentration. Overall, the influence of KOH concentration on the polarization curves is well captured by the simulations well. Nevertheless, if the simulated polarization curve obtained for a KOH concentration of 0.5 M (solid blue line in Figure 2) slightly deviates from the experimental data at low-current density, quite good agreement with the measurements is achieved at high current density for the other KOH concentrations. Indeed, for low current, our 3D model overestimates the performance obtained by Liu et al. [20] except for a KOH concentration of 0.01 M (solid orange line in Figure 2). The deviation between our 3D model and data from Liu et al.'s study can be attributed to differences in cell geometry, namely the triple serpentine flow-fields used by Liu et al. [20].

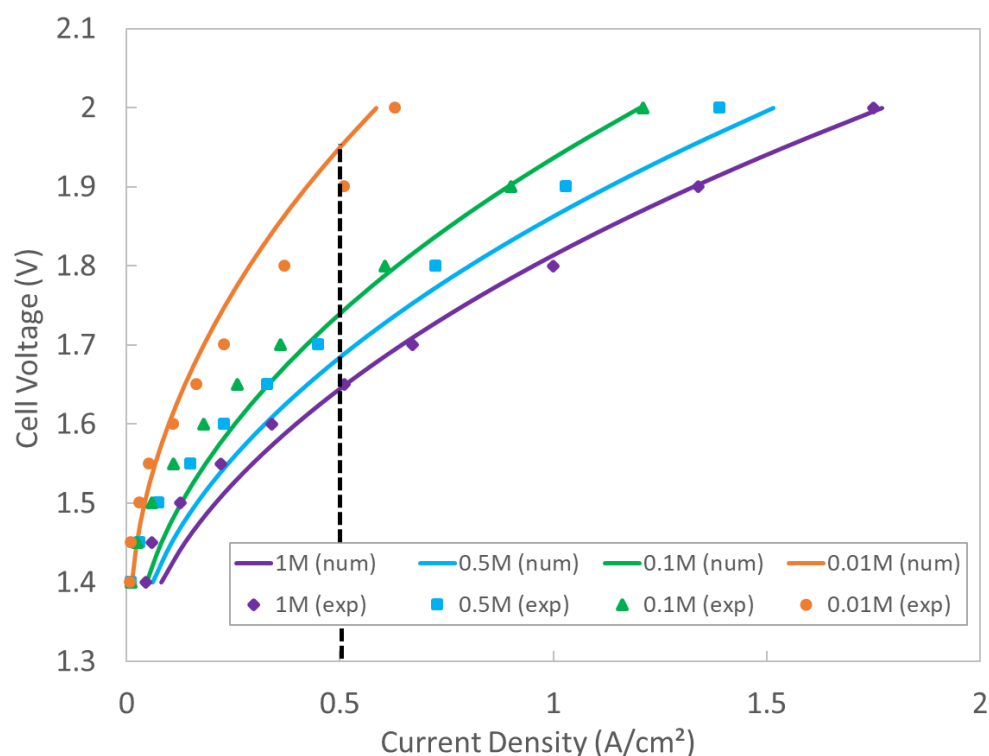


Figure 2. Numerical polarization curves at 60 °C and 1 atm, for a KOH solution flow rate of 100 mL/min (solid lines) and experimental data from Liu et al.'s study [20] (symbols). The dashed line refers to a cell current density of 0.5 A/cm².

Figure 3 shows the total volumetric reaction current as well as the ionic and electronic potential distributions from the catalyst layer/membrane interface through the anode and cathode CL thickness at the middle of the cell length (green dashed line in Figure 1) at a cell current density of 0.5 A/cm² (dashed line in Figure 2) for different electrolyte concentrations. As the KOH concentration decreases, the local volumetric current density and ionic potential gradients increase while the electronic potential distribution remains almost uniform over the entire CL thickness. Volumetric current densities and ionic poten-

tial both exhibit higher gradients close to the catalyst layer/membrane interface. Indeed, ionic ohmic drop limitation becomes predominant when lowering the KOH concentration, reducing the catalyst utilization rate while the electronic conductors act as an equipotential. Under a KOH flow rate of 100 mL/min and at an applied current density of 0.5 A/cm^2 , the shapes of the current density distribution are quite different from the ones predicted by Liu et al.'s 1D model [20] except at high KOH concentration. This difference is likely due to the fact that we assume a constant electrochemical surface area whatever the KOH concentration. It is also worth mentioning that the current density distributions do not change significantly along the channel length from the inlet to the outlet as the flow rate is quite high in this first case. Moreover, no rib/channel effects were noticed as the straight channel shape was considered.

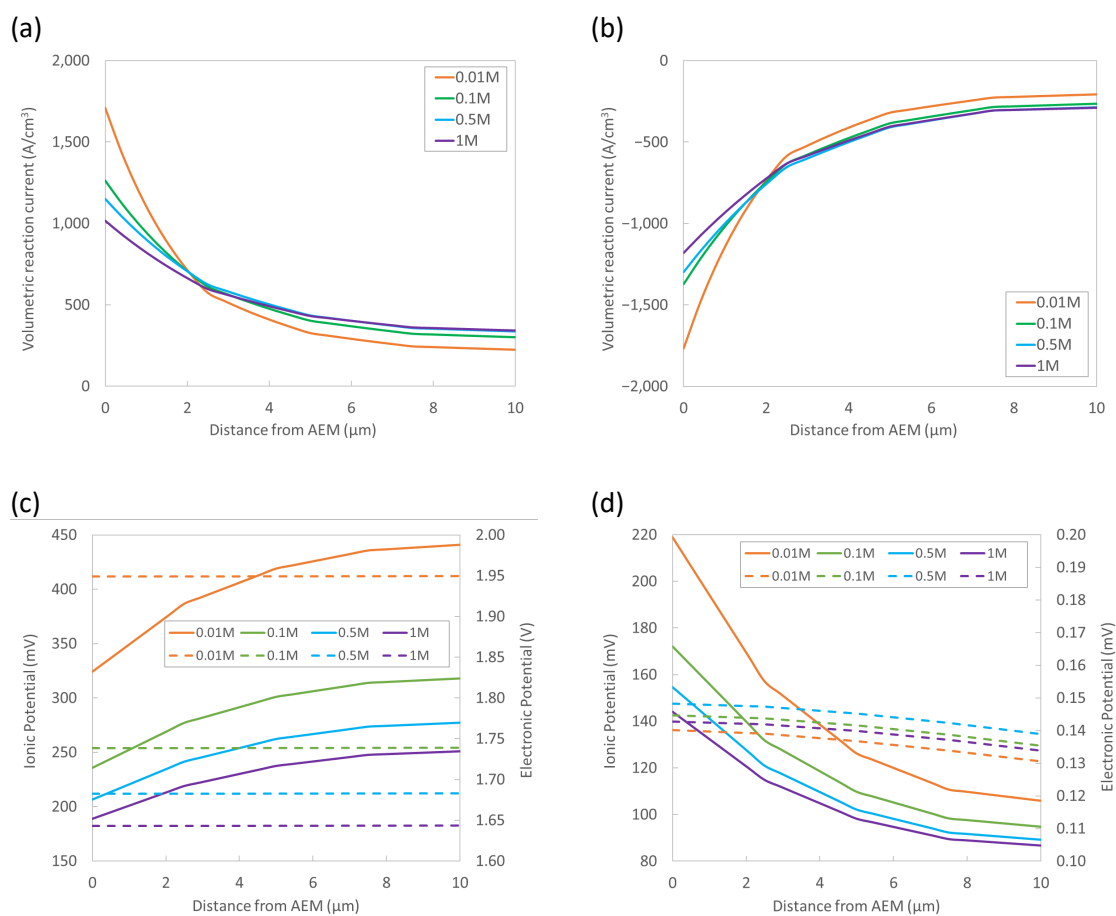


Figure 3. Total volumetric reaction current through the: (a) anode CL thickness and (b) cathode CL thickness at a cell current density of 0.5 A/cm^2 (black dashed line in Figure 2) for different KOH concentrations at 50% of the cell length (green dashed line in Figure 1). Electronic (dashed curves) and ionic (solid curves) potential distributions through the: (c) anode CL thickness and (d) cathode CL thickness at a cell current density of 0.5 A/cm^2 (black dashed line in Figure 2) for different KOH concentrations at 50% of the cell length (green dashed line in Figure 1). Abscissa 0 refers to the AEM/ACL or AEM/CCL interface.

Figure 4a shows the H_2 and O_2 gaseous volume fraction distribution at 2 V (i.e., at the maximum current density) for all of the KOH concentrations in porous media (i.e., CL and PTL) and gas channels. This latter is displayed along the cell length thanks to a through-plane cut in the middle of the cell (i.e., the red zone in Figure 1). The cuts respect an aspect ratio of one-quarter in length for better visibility with the inlet flow of the KOH solution at the bottom and the outlet at the top. The cathode compartment (channel-CPTL-CCL) is represented on the left of each cut, where HER takes place (negative electrode), and

the anodic compartment (ACL-APTL-channel) on the right, where OER occurs (positive electrode). At low concentrations, the gas volume fraction is truly uniform along the porous layers and the gas channel because the current density is low, which consequently results in less gas production. It becomes heterogeneous at higher current densities when the KOH concentration increases. Finally, Figure 4b shows the gaseous volume fraction at different cell voltages at 1 M KOH. As in the previous case, gas production becomes more heterogeneous when increasing the cell voltage (i.e., increasing the current density) because of the gaseous volume fraction accumulation along the cell length on the flow direction.

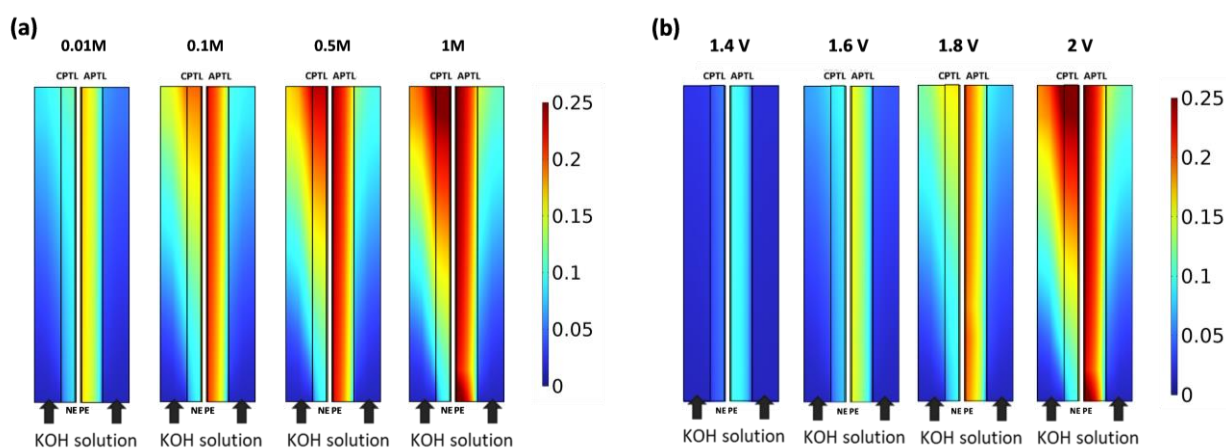


Figure 4. Gaseous volume fraction for: (a) various KOH concentrations (i.e., 0.01, 0.1, 0.5, and 1 M) at 2 V and (b) different cell voltages (i.e., 1.4, 1.6, 1.8, and 2 V) at 1 M along the cell length in the middle of the cell (i.e., the red zone in Figure 1). The cuts respect an aspect ratio of one-quarter in length for better visibility. NE: negative electrode, PE: positive electrode.

Liu et al.'s model was extended to be able to forecast the through-plane and in-plane gas distribution in the different layers of the cell. At a flow rate of 100 mL/min, the gas volume fraction distribution becomes strongly non-uniform at a current density above 1 A/cm² (corresponding to a cell voltage of 1.8 V at 1 M and 2 V at 0.1 M). The gas phases accumulate both in the PTL and the channel. The gas volume fraction is also more heterogeneous at the cathode (H₂) than at the anode (O₂). Regardless of the concentration, oxygen tends to stagnate more than hydrogen in its respective porous media. This can be explained by the higher density of oxygen compared to hydrogen, as well as an anode PTL that is one-third thicker (but with the same porosity) than the cathode PTL (Tables 2 and 5). In the channel, the gas phases accumulate along the cell length from the inlet toward the outlet because of the electrolyte flows. Nevertheless, the impact of the two-phase flow is quite small when considering a high electrolyte flow rate. Therefore, a flow rate ten times lower is considered in the next section.

3.2. Flow Rate Study

Figure 5 shows the total volumetric reaction current through the anode catalyst layer and cathode catalyst layer at the middle of the cell length (the green dashed line in Figure 1) at a cell current density of 0.5 A/cm² for two different flow rates, namely 100 mL/min (solid curves) and 10 mL/min (dashed curves). Even if the flow rate of the KOH solution is ten times lower, the volumetric reaction current through the anode and cathode catalyst layers' thickness at a cell current density of 0.5 A/cm² remains similar to the one obtained at a higher flow rate. Indeed, the bubble overpotential contribution is not so important when noble catalysts are used. The electrochemical reaction kinetics are fast enough to maintain performance. Liu et al.'s simulations confirm a quite small bubble overpotential lower than 50 mV even at high-current density [20].

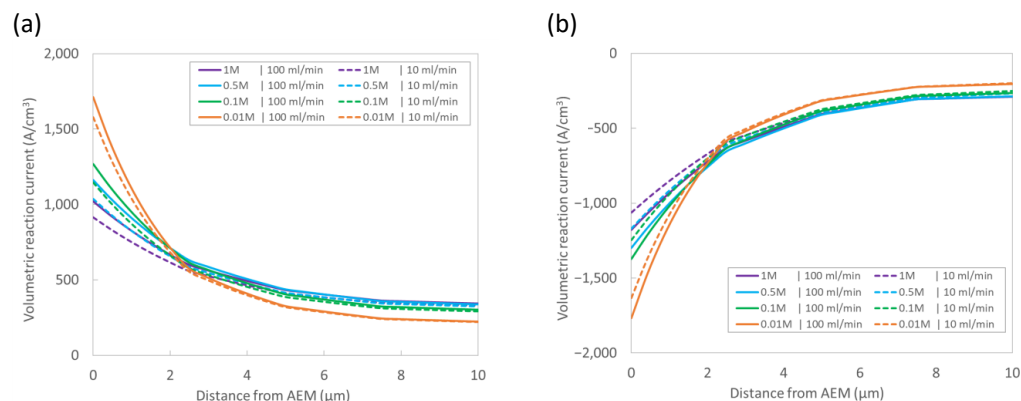


Figure 5. Total volumetric reaction current through the: (a) anode catalyst layer and (b) cathode catalyst layers' thickness at the middle of the cell length (the green dashed line in Figure 1) at a cell current density of 0.5 A/cm^2 for different KOH concentrations for flow rates of 100 mL/min (solid curves) and 10 mL/min (dashed curves).

To go further in our understanding of flow rate impact, Figure 6 shows the polarization curves for different KOH concentrations and the gaseous volume fraction for 1 M at 1.55 A/cm^2 for flow rates of 10 mL/min and 100 mL/min . Surprisingly, the performance of the AEMWE cell does not deteriorate so much when dividing the flow rate by ten (Figure 6a). Indeed, the cell voltage change does not exceed 100 mV in the worst situation (at 1.5 A/cm^2 which can be achieved only in 1 M KOH) despite the very inhomogeneous distribution of the gaseous volume fraction distribution along the channel length at a lower flow rate (Figure 6b). At a lower electrolyte flow rate, the gaseous volume fraction can reach high values at the channel outlet (0.7 at the cathode and 0.5 at the anode at a KOH concentration of 1 M) with a relative effect on cell performance. Moreover, the larger conversion ratio of water to H_2 and O_2 also induces a strongly non-uniform current density distribution through the catalyst layer thicknesses (Figure 7a,b). Nonetheless, these heterogeneities remain relatively small as the anode and cathode overpotential partly contribute to cell polarization when PGM catalysts are used. Indeed, the fast HER kinetics on the Pt catalyst are only slightly influenced by the decrease in the active surface area caused by the H_2 gaseous volume fraction. This non-uniform distribution may be more pronounced if PGM-free catalysts are used because of the necessity of a thicker catalyst layer in order to compensate for lower catalyst activity. Figure 7c,d displays the gaseous volume fraction for flow rates of 10 mL/min through the catalyst layer thickness. As the catalyst layer is thin with a PGM catalyst, no significant gradient can be observed even at a low flow rate.

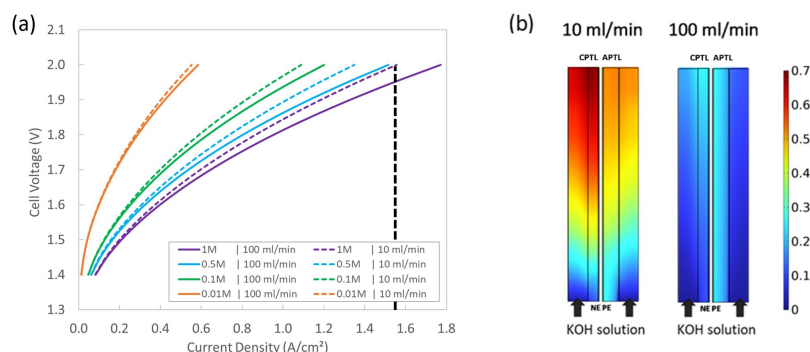


Figure 6. (a) Polarization curves for different KOH concentrations for flow rates of 100 mL/min (solid curves) and 10 mL/min (dashed curves). (b) Gaseous volume fraction for 1 M at 1.55 A/cm^2 (dashed line in (a)) for flow rates of 10 mL/min (left) and 100 mL/min (right) according to a through-plane cut along the channel at the middle of the cell (red zone in Figure 1). The cuts respect an aspect ratio of one-quarter in length for better visibility. NE: negative electrode, PE: positive electrode.

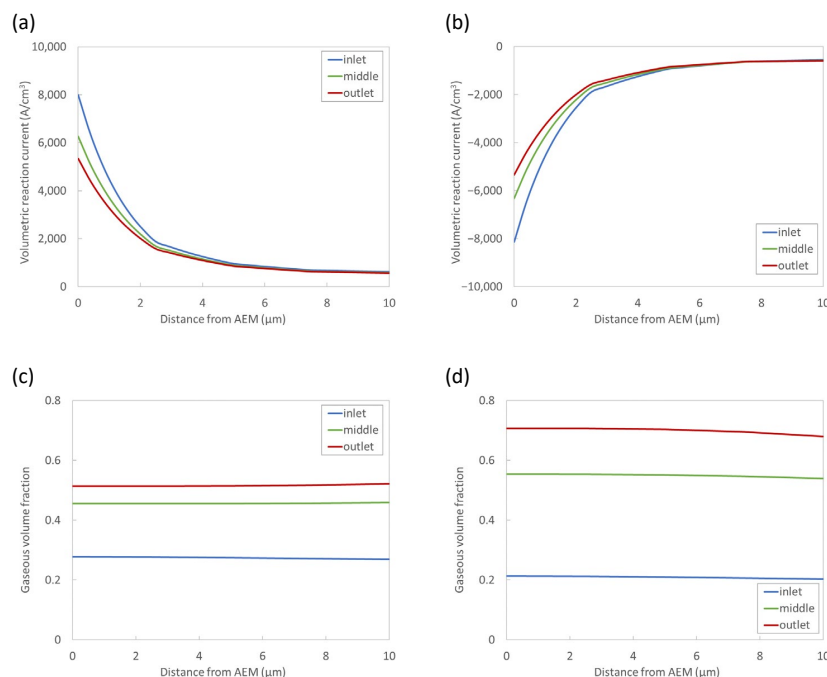


Figure 7. Total volumetric reaction current through the: (a) anode catalyst layer and (b) cathode catalyst layer thickness at the inlet (blue), middle (green), and outlet (red) of the cell length (blue, green, and red dashed lines in Figure 1) at a cell current density of 1.55 A/cm^2 (black dashed line in Figure 6a) for a flow rate of 10 mL/min for a KOH concentration of 1 M . Gaseous volume fraction through the: (c) anode catalyst layer and (d) cathode catalyst layer thickness at the inlet (blue), middle (green), and outlet (red) of the cell length (blue, green, and red dashed lines in Figure 1) at a cell current density of 1.55 A/cm^2 (black dashed line in Figure 6a) for a flow rate of 10 mL/min for a KOH concentration of 1 M . Abscissa 0 refers to the AEM/ACL or AEM/CCL interface.

4. Conclusions

AEMWEs have the potential to be an efficient and environmentally friendly method for producing hydrogen fuel. Nonetheless, they face certain constraints that could limit their practicality in certain scenarios. Hence, modeling proves to be a valuable approach for understanding and optimizing the performance of these systems.

In this work, a 3D two-phase flow multi-physics model of an anion exchange membrane water electrolyzer is developed to investigate the concentration influence of a potassium hydroxide electrolyte. The model was validated through comparison with Liu et al.'s experimental data obtained at different concentrations [20]. The simulated AEMWE polarization curves for various KOH concentrations are in good agreement with the experimental data. In the case of the 10 μm thick catalyst layer, the model predicts the appearance of strongly non-uniform H_2 and O_2 gas volume distributions for current densities above 1 A/cm^2 . The impact of H_2 and O_2 gas production and transport was investigated. The performance of AEMWE cells varies locally along the channel due to changes in gas volume fraction distribution, namely at high current density and low electrolyte flow rate, reducing the catalyst utilization rate. According to the simulations performed in 1 M KOH flowing at 10 mL/min and at an applied current density of 1.55 A/cm^2 , the gas volume fraction reaches 0.7 at the cathode (H_2) and 0.5 at the anode (O_2). Nevertheless, in the case of the PGM catalyst, the impact of the gas volume fraction is limited due to the fast electrochemical HER and OER reactions as well as the thin catalyst layer. The influence of the two-phase flow distribution will likely become more detrimental when PGM-free catalyst layers are used due to the use of thicker electrodes. Bubble overpotential may strongly increase, reducing catalyst layer utilization and cell performance. Therefore, the influence of bubble formation on the specific active surface area needs to be better understood. This topic is very tricky in alkaline membrane electrolyzers and requires intense research.

Supplementary Materials: The following supporting information can be downloaded at: <https://www.mdpi.com/article/10.3390/en17133238/s1>, Figure S1: Two different element mesh refinements: (a) 46,880 hexahedral elements and (b) 356,288 hexahedral elements; Figure S2: Numerical polarization curves at 60 °C and 1 atm. for a KOH solution flow rate of 100 mL/min and a KOH concentration of 1 M according different level of finite element mesh refinement.

Author Contributions: Conceptualization, E.T., F.D. and A.B.; methodology, F.D., A.B., M.G. and B.L.; software, E.T.; validation, E.T. and Y.B.; formal analysis, E.T., F.D., A.B., M.G. and B.L.; investigation, E.T., F.D., A.B., M.G. and B.L.; resources, F.D.; data curation, E.T.; writing—original draft preparation, E.T. and Y.B.; writing—review and editing, E.T. and Y.B.; visualization, E.T.; supervision, F.D.; project administration, F.D.; funding acquisition, F.D. All authors have read and agreed to the published version of the manuscript.

Funding: Financial support for this work provided by the tire manufacturing company Michelin is gratefully acknowledged.

Data Availability Statement: The original contributions presented in the study are included in the article/Supplementary Material, further inquiries can be directed to the corresponding author.

Conflicts of Interest: The authors declare no conflicts of interest.

Nomenclature

ACL	Anode catalyst layer
AEM	Anion exchange membrane
AEMWE	Anion exchange membrane water electrolyzer
APTL	Anode porous transport layer
CCL	Cathode catalyst layer
CL	Catalyst layer
CPTL	Cathode porous transport layer
GHG	Greenhouse gas
HER	Hydrogen evolution reaction
MEA	Membrane electrode assembly
NE	Negative electrode
OER	Oxygen evolution reaction
PE	Positive electrode
PEM	Proton exchange membrane
PEMWE	Proton exchange membrane water electrolyzer
PFAS	Polyfluoroalkyl polymer
PGMs	Platinum-group metals

List of Symbols

Latin

a_v	Electrocatalyst specific surface area	m^2/m^3
c_{OH^-}	Hydroxide concentration	mol/m^3
c_t	Concentration of the fixed positive charge in the ionomer	mol/m^3
C_{p1}	Heat capacity of liquid water	$J/(g \cdot K)$
d_{CK}	Characteristic diameter	μm
E_{eq}	Equilibrium potential	V
EW	Equivalent weight	kg/mol
F	Faraday's constant	C/mol
H_l	Enthalpy of liquid water	J/g
i	Current density	A/cm^2
i_0	Exchange current density	mA/cm^2
i_v	Volumetric reaction current	A/cm^3
I	Identity matrix	–
IEC	Ion exchange capacity	mmol/g
$J(s_l)$	Leverett J-function (liquid volume fraction dependent)	–
k_{CK}	Empirical geometric constant (Cozeny–Karman)	–

k_{ml}	Rate constant for the water transfer from the ionomer to the liquid phase	$\text{g}\cdot\text{mol}/(\text{cm}^3\cdot\text{s}\cdot\text{J})$
k_r	Relative permeability	–
k_{sat}	Absolute permeability	m^2
M	Molar mass	kg/mol
$N_{\text{H}_2\text{O},i}$	Water molar flux through the ionomer	$\text{mol}/(\text{m}^2\cdot\text{s})$
p	Pressure	Pa
p_c	Capillary pressure	Pa
R	Universal gas constant	$\text{J}/(\text{mol}\cdot\text{K})$
$R_{\text{H}_2\text{O}}$	Rate of water production (anode) or consumption (cathode)	$\text{mol}/(\text{m}^3\cdot\text{s})$
R_k	Source term of phase k for mass conservation	$\text{kg}/(\text{m}^3\cdot\text{s})$
R_{ml}	Rate of water absorption or desorption from the ionomer to the liquid phase	$\text{mol}/(\text{m}^3\cdot\text{s})$
s_k	Volume fraction of phase k	–
T	Temperature	K
u	Velocity	m/s
\bar{V}_l	Molar volume of liquid water	mL/mol
z^+	Positive charge	–
z^-	Charge of hydroxide ions	–
Greek		
α	Charge transfer coefficient for oxidation	–
α_l	Liquid-equilibrated water transport coefficient	–
β	Charge transfer coefficient for reduction	$\text{s}\cdot\text{mol}^2/(\text{kg}\cdot\text{m}^3)$
ε	Porosity	–
ε_e	Volume fraction of the electronically conductive phase	–
ε_i	Volume fraction of the ionomer phase	–
η	Overpotential	V
θ	Contact angle	°
μ	Dynamic viscosity	$\text{Pa}\cdot\text{s}$
$\mu_{\text{H}_2\text{O},i}$	Chemical potential of water absorbed in the ion-conducting phase	J/mol
μ_{liq}	Chemical potential of liquid water	J/mol
ξ	Electroosmotic coefficient	–
ρ	Density	kg/m^3
σ	Surface tension	mN/m
σ_e	Electronic conductivity	S/cm
σ_i	Ionic conductivity	S/cm
Φ_e	Electronic potential	V
Φ_i	Ionic potential	V
Superscripts and Subscripts		
a	Anodic	
bulk	Bulk	
c	Cathodic	
e	Electronic	
eff	Effective	
HER	Hydrogen evolution reaction	
H_2	Hydrogen	
H_2O	Water	
g	Gas	
k	Phase	
l	Liquid	
m	Mixture	
OER	Oxygen evolution reaction	
O_2	Oxygen	
ref	Reference	
t	Triple-point	

References

1. Chatenet, M.; Pollet, B.G.; Dekel, D.R.; Dionigi, F.; Deseure, J.; Millet, P.; Braatz, R.D.; Bazant, M.Z.; Eikerling, M.; Staffell, I.; et al. Water electrolysis: From textbook knowledge to the latest scientific strategies and industrial developments. *Chem. Soc. Rev.* **2022**, *51*, 4583–4762.
2. Du, N.; Roy, C.; Peach, R.; Turnbull, M.; Thiele, S.; Bock, C. Anion-Exchange Membrane Water Electrolyzers. *Chem. Rev.* **2022**, *122*, 11830–11895. [[CrossRef](#)]
3. Makhsoos, A.; Kandidayeni, M.; Pollet, B.G.; Boulon, L. A perspective on increasing the efficiency of proton exchange membrane water electrolyzers—A review. *Int. J. Hydrogen Energy* **2023**, *48*, 15341–15370. [[CrossRef](#)]
4. Hamid, N.; Junaid, M.; Manzoor, R.; Sultan, M.; Meng Chuan, O.; Wang, J. An integrated assessment of ecological and human health risks of per- and polyfluoroalkyl substances through toxicity prediction approaches. *Sci. Total Environ.* **2023**, *905*, 167213. [[CrossRef](#)]
5. Xu, Q.; Zhang, L.; Zhang, J.; Wang, J.; Hu, Y.; Jiang, H.; Li, C. Anion Exchange Membrane Water Electrolyzer: Electrode Design, Lab-Scaled Testing System and Performance Evaluation. *Energy Chem.* **2022**, *4*, 100087. [[CrossRef](#)]
6. Faid, A.Y.; Xie, L.; Barnett, A.O.; Seland, F.; Kirk, D.; Sunde, S. Effect of anion exchange ionomer content on electrode performance in AEM water electrolysis. *Int. J. Hydrogen Energy* **2020**, *45*, 28272–28284. [[CrossRef](#)]
7. Shirvastian, P.; Loh, A.; Sluijter, S.; Li, X. Novel components in anion exchange membrane water electrolyzers (AEMWE's): Status, challenges and future needs. A mini review. *Electrochem. Commun.* **2021**, *132*, 107140. [[CrossRef](#)]
8. Yu, R.; Yang, H.; Yu, X.; Cheng, J.; Tan, Y.; Wang, X. Preparation and research progress of anion exchange membranes. *Int. J. Hydrogen Energy* **2024**, *50*, 582–604. [[CrossRef](#)]
9. Yuan, S.; Zhao, C.; Cai, X.; An, L.; Shen, S.; Yan, X.; Zhang, J. Bubble evolution and transport in PEM water electrolysis: Mechanism, impact, and management. *Prog. Energy Combust. Sci.* **2023**, *96*, 101075. [[CrossRef](#)]
10. Angulo, A.; van der Linde, P.; Gardeniers, H.; Modestino, M.; Fernández Rivas, D. Influence of bubbles on the energy conversion efficiency of electrochemical reactors. *Joule* **2020**, *4*, 555–579. [[CrossRef](#)]
11. Zhao, X.; Ren, H.; Luo, L. Gas bubbles in electrochemical gas evolution reactions. *Langmuir* **2019**, *35*, 5392–5408. [[CrossRef](#)]
12. Bonnefont, A.; Ryabova, A.S.; Schott, T.; Kéranguéven, G.; Istomin, S.Y.; Antipov, E.V.; Savinova, E.R. Challenges in the Understanding Oxygen Reduction Electrocatalysis on Transition Metal Oxides. *Curr. Opin. Electrochem.* **2019**, *14*, 23–31. [[CrossRef](#)]
13. Chand, K.; Paladino, O. Recent developments of membranes and electrocatalysts for the hydrogen production by anion exchange membrane water electrolyzers: A review. *Arab. J. Chem.* **2023**, *16*, 104451. [[CrossRef](#)]
14. Lee, C.H.; Lee, J.K.; Zhao, B.; Fahy, K.F.; Bazylak, A. Transient gas distribution in porous transport layers of polymer electrolyte membrane electrolyzers. *J. Electrochem. Soc.* **2020**, *167*, 024508. [[CrossRef](#)]
15. Majasan, J.O.; Cho, J.I.S.; Dedigama, I.; Tsaoulidis, D.; Shearing, P.; Brett, D.J.L. Two-phase flow behaviour and performance of polymer electrolyte membrane electrolyzers: Electrochemical and optical characterisation. *Int. J. Hydrogen Energy* **2018**, *43*, 15659–15672. [[CrossRef](#)]
16. Lee, J.K.; Lee, C.; Fahy, K.F.; Zhao, B.; LaManna, J.M.; Baltic, E.; Jacobson, D.L.; Hussey, D.S.; Bazylak, A. Critical current density as a performance indicator for gas-evolving electrochemical devices. *Cell Rep. Phys. Sci.* **2020**, *1*, 100147. [[CrossRef](#)]
17. Li, Z.; Wang, C.; Li, L.; Wu, J.; Yin, Z.; Tan, D. Numerical investigation of mesoscale multiphase mass transport mechanism in fibrous porous media. *Eng. Appl. Comput. Fluid Mech.* **2024**, *18*, 2363246. [[CrossRef](#)]
18. Daoudi, C.; Bounahmidi, T. Overview of alkaline water electrolysis modeling. *Int. J. Hydrogen Energy* **2024**, *49*, 646–667. [[CrossRef](#)]
19. An, L.; Zhao, T.S.; Chai, Z.H.; Tan, P.; Zeng, L. Mathematical modeling of an anion-exchange membrane water electro-lyzer for hydrogen production. *Int. J. Hydrogen Energy* **2014**, *39*, 19869–19876. [[CrossRef](#)]
20. Liu, J.; Kang, Z.; Li, D.; Pak, M.; Alia, S.M.; Fujimoto, C.; Bender, G.; Kim, Y.S.; Weber, A.Z. Elucidating the Role of Hydroxide Electrolyte on Anion-Exchange-Membrane Water Electrolyzer Performance. *J. Electrochem. Soc.* **2021**, *168*, 054522. [[CrossRef](#)]
21. Lawand, K.; Sampathkumar, S.N.; Mury, Z.; Van Herle, J. Membrane electrode assembly simulation of anion exchange membrane water electrolysis. *J. Power Sources* **2024**, *595*, 234047. [[CrossRef](#)]
22. Gerhardt, M.L.; Pant, L.M.; Weber, A.Z. Along-the-Channel Impacts of Water Management and Carbon-Dioxide Contamination in Hydroxide-Exchange-Membrane Fuel Cells: A Modeling Study. *J. Electrochem. Soc.* **2019**, *166*, F3180–F3192. [[CrossRef](#)]
23. Weber, A.Z.; Newman, J. Transport in Polymer-Electrolyte Membranes: II. Mathematical Model. *J. Electrochem. Soc.* **2004**, *151*, A311. [[CrossRef](#)]

Disclaimer/Publisher's Note: The statements, opinions and data contained in all publications are solely those of the individual author(s) and contributor(s) and not of MDPI and/or the editor(s). MDPI and/or the editor(s) disclaim responsibility for any injury to people or property resulting from any ideas, methods, instructions or products referred to in the content.